nature communications

Article

https://doi.org/10.1038/s41467-025-56477-7

Enhanced phosphorus weathering contributed to Late Miocene cooling

Received: 20 June 2024

Accepted: 15 January 2025

Published online: 28 January 2025

Check for updates

Yi Zhong[1,2], Zhiguo Li[3], Xuefa Shi[4], Terry Isson[5], Jimin Yu[6,7,8], Sev Kender[9], Zhou Liang[10], George E. A. Swann[11], Alex Pullen[12], Michael E. Weber[13], Jinlong Du[14], Juan C. Larrasoaña[15,16], Jingyu Zhang[1], Yafang Song[17], F. J. González[18], Stefanie Kaboth-Bahr[19], Hai Li[20], Qi Zhang[21], Debo Zhao[22], Wei Cao[1], Mingyu Zhao[23] & Qingsong Liu[1,24]

Late Miocene climate evolution provides an opportunity to assess Earth's climate sensitivity to carbon cycle perturbation under warmer-than-modern conditions. Despite its relevance for understanding the climate system, the driving mechanisms underlying profound climate and carbon cycle changes – including the enigmatic Late Miocene cooling from 7 to 5.4 million years ago – remain unclear. Here, we present magnetic and geochemical paleoceanographic proxies from a hydrogenetic ferromanganese crust retrieved in the northwestern Pacific Ocean. Our results indicate a striking 50% surge in deep ocean phosphorus concentrations occurred 7 – 4 million years ago, synchronous with enhanced deep ocean oxygen consumption. Employing a global biogeochemical model, we show that increased continental phosphorus weathering, without a concurrent rise in silicate weathering, contributed to the decline in atmospheric CO_2 and associated cooling over the Late Miocene. This suggests a prominent decoupling of phosphorus and silicate weathering during a major carbon cycling event over the last 10 million years.

The Late Miocene, 11.6 to 5.3 million years ago (Ma), is a time period that witnessed significant global changes in tectonics, biological communities, and climate, including the so-called Late Miocene cooling (LMC) that resulted in the establishment of near-modern ocean temperatures between 7 and 5.4 Ma[1,2]. During this time, ocean temperatures decreased substantially in deep and shallow waters as part of the long-term Cenozoic cooling and atmospheric CO_2 decline[3–5]. This period offers a unique opportunity to investigate interactions of climate and global carbon cycling under a warmer-than-modern condition, potentially providing valuable information to inform models and thereby improving predictions related to climate change and terrestrial ecosystem responses[6–9].

Reconstructions of sea surface temperatures (SST) highlight significant cooling in both hemispheres between 7 and 5.4 Ma[1,2]. A global carbon isotope ($\delta^{13}C$) excursion occurred during the Late Miocene that reveals carbon cycle dynamics involving the terrestrial and deep ocean carbon reservoirs, thought to drive Late Miocene climate cooling[2]. However, the dynamic processes and driving forces underlying the LMC are debated[10]. Some studies suggest that a gradual decline in atmosphere CO_2 played a central role in driving global cooling[11] and associated changes in terrestrial ecosystems[12,13]. However, the role of enhanced silicate and phosphorus (P) weathering during the LMC is less clear[14–16]. Silicate weathering, if coupled to carbonate formation (as opposed to clay synthesis), contributes to the net consumption of ocean-atmospheric CO_2[17–21], while P cycling affects atmospheric CO_2 by regulating oceanic productivity and organic matter burial[22–24]. In this study, we investigate the relative roles of silicate weathering and P cycling in regulating the global climate over the LMC.

In this study, we use phosphorous-to-iron ratio (P/Fe) records of a hydrogenetic ferromanganese crust from the West Pacific (Fig. 1 and Supplementary Fig. 1) to infer oceanic P concentrations and continental P weathering during the Late Miocene. By employing a global biogeochemical model, we demonstrate that increased P weathering alone suffices to lower atmospheric CO_2 and explain the LMC.

A full list of affiliations appears at the end of the paper. e-mail: zhongy@sustech.edu.cn; mingyu.zhao@mail.iggcas.ac.cn; qsliu@sustech.edu.cn

https://doi.org/10.1038/s41467-025-56477-7

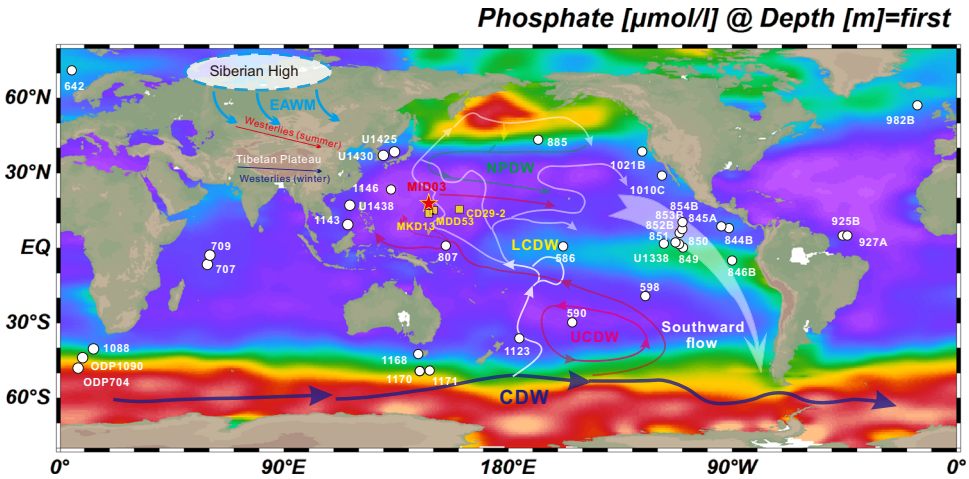

Fig. 1 | Modern surface ocean phosphate and general deep Pacific Ocean circulation patterns (modified from ref. 89). Fe-Mn crust MID03 (red star), ODP/DSDP sites (white circles) and Fe-Mn crust (yellow square) are plotted in this figure. Detailed information about these deposits are provided in Supplementary Table 1. Yellow and red circles with a central point represent the upwelling of Lower Circumpolar Deep Water (LCDW) and Upper Circumpolar Deep Water (UCDW), respectively (modified from refs. 90,89). The white arrow shows the flow carrying modified North Pacific Deep Water (NPDW) to mix with UCDW. Arrows indicate wind directions for the East Asian Winter Monsoon (EAWM; light blue) and the prevailing westerlies (dark blue arrow over land for winter; pink arrow over land for summer; thick red arrow over the ocean). The figure was created with Ocean Data View[91].

Contrary to the traditional view that assumes a direct coupling between P and silicate weathering, we posit that these processes may have undergone different dynamics during the LMC.

Results and discussion

Shifts in oceanic P reservoir and primary productivity

Phosphorus cycling plays a prominent role in regulating oceanic primary production on various time scales, with profound impacts on oceanic biogeochemistry, ecosystem structure, and global climate[22,25,26]. In all modern aquatic systems, phosphorus is primarily sourced from the weathering of continental materials[27,28]. Key processes responsible for the internal recycling of dissolved phosphate include mixing of the surface and deep oceans, and the release of organic phosphorus back into the deeper ocean[22].

At site MID03 from the North Pacific, crust samples are hydrogenetic (Supplementary Figs. 2 and 3 and Supplementary Text 1), reflecting genesis from cold, deep water. In this crust, Fe_2O_3 and P_2O_5 show a strong positive correlation, while a significant inverse relationship is observed between MnO_2 and P_2O_5 (Supplementary Fig. 4 and Supplementary Tables 3 and 4). This indicates that P is mainly hosted in iron oxyhydroxides of the ferromanganese crust. Previous studies have revealed that P/Fe of iron oxyhydroxide precipitates are strongly correlated with ambient deep-water phosphate levels[29–32]. We build on these previous studies[31,32] by employing P from iron-oxyhydroxide P/Fe ratios in crust MID03 as a proxy for past deep-water phosphate levels.

Our results indicate a pronounced increase in oceanic P concentrations during the Late Miocene (Fig. 2d), with P/Fe ratios increasing from ca. 0.032 to around 0.046 between 7.5 and 4 Ma, followed by a notable decrease from about 0.046 to 0.035 between 4 and 3 Ma. P/Fe further increases to 0.042 at 2 Ma and then decreases to 0.038 at 1 Ma after which it remains roughly stable into the Pleistocene (Supplementary Fig. 5b). The modern deep-sea P concentration is comparatively homogeneous at ~3 μM[33], although we note that small variations in P are documented globally, especially in the Pacific Ocean (Fig. 3c)[15,34–37]. We suggest that P/Fe changes in our MID03 crust possibly reflect a whole deep ocean P shift during the Late Miocene. Therefore, we calculated the evolution of deep ocean P concentrations over the past 10 Myrs using the P/Fe record (Fig. 4).

Our reconstructed rise in oceanic P concentrations can well explain a previously documented productivity enhancement observed at multiple locations during the Late Miocene. For example, previous studies have shown increased opal accumulation at ODP 885/886 (Fig. 2b) and barium enrichment (Ba_{EF}; an established productivity proxy) in the Sea of Japan (Fig. 2c)[38]. The widespread and prolonged productivity peak in the low-latitude Pacific Ocean during the Late Miocene also aligns with a "biogenic bloom" in the eutrophic upwelling systems of the Indian[37] and Pacific oceans[39] (Fig. 2f and Supplementary Table 1). Specifically, in the eastern equatorial Pacific[40] and Southern Ocean[41], opal and paleoproductivity deposition (Fig. 2e and g) reached a peak between 7.0 and 6.4 Ma[42,43] and declined after that until ~4 Ma. Given that P is a crucial limiting nutrient for primary productivity[44,45], we propose that increased oceanic P levels were a main forcing of enhanced primary productivity beginning in the Late Miocene.

Nutrient cycling dynamics

Iron, phosphorus, and nitrogen are essential nutrients for phytoplankton growth and carbon sequestration[46]. Late Miocene phosphatization has also been observed along Western Pacific[47,48] Chatham Rise[49,50], Blake Plateau[51], southwest Africa[52], northwestern Iberia[53], and southern California[54]. Major climatic shifts were thought to have initiated ocean phosphogenesis by promoting intense oceanic vertical mixing that mobilized a large amount of phosphorus previous stored in the deep ocean[55].

To assess ocean circulation and upwelling processes over the LMC, we use the εNd recorded in crust MID03 and other samples from the West Pacific as a water mass tracer[56,57]. Our crusts from the West Pacific show a relatively radiogenic Nd isotope composition during the Late Miocene (Supplementary Fig. 5e and Fig. 7b), with consistency between lead and iron isotope data suggesting they are affected by similar changes in the source province[58]. The increase in εNd during 8–4 Ma likely indicates enhanced input of more radiogenic island arc materials at low latitudes[58], pointing to a shift from marginal northwest Pacific deep waters to low-latitude equatorial deep waters in the region. We propose that climate cooling and the formation of Pacific deep water influenced deep-water upwelling in the Western Pacific during the Late Miocene[38]. These deep-water oscillations likely enhanced nutrient circulation within

https://doi.org/10.1038/s41467-025-56477-7

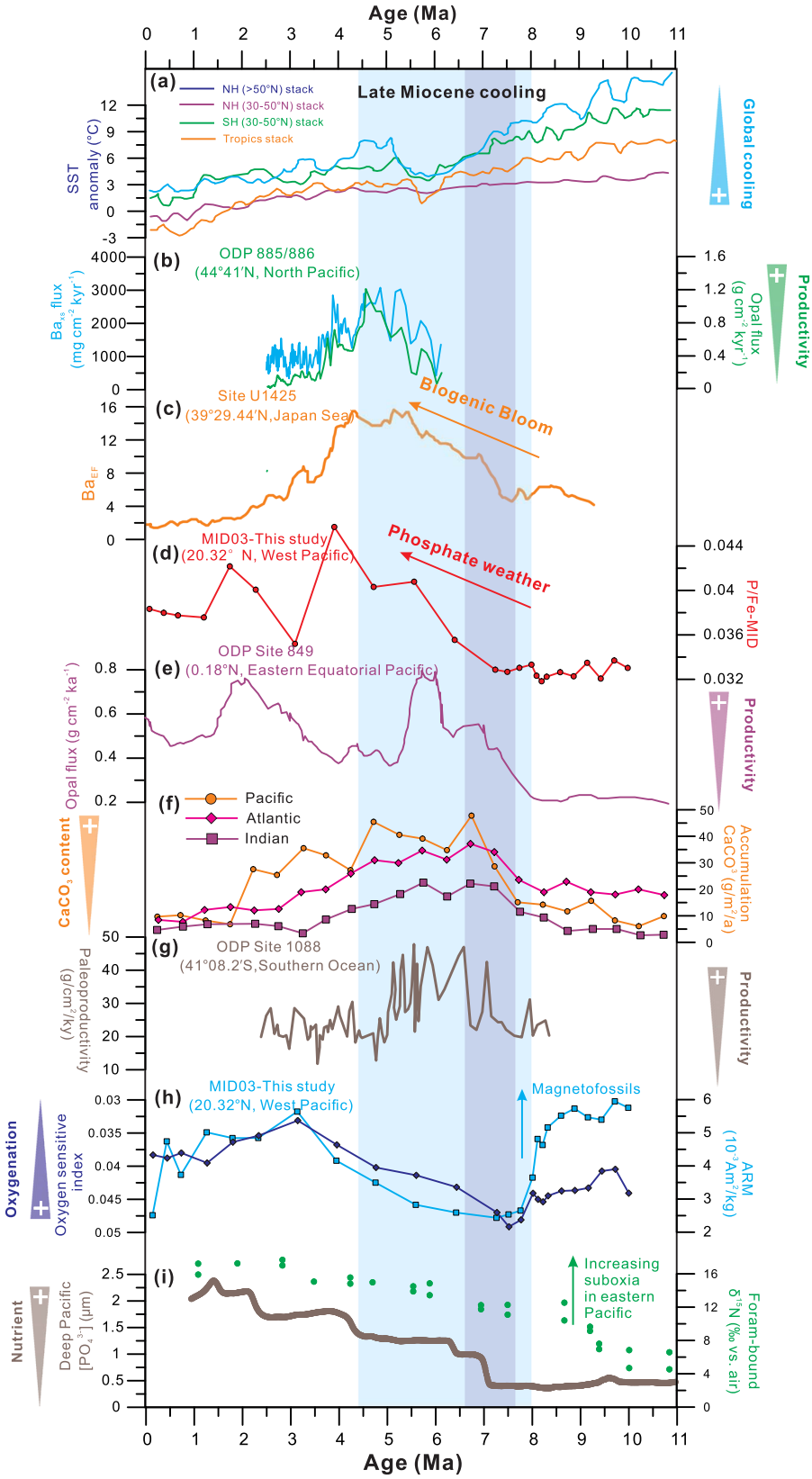

Fig. 2 | Proxy records of nutrient utilization and paleoproductivity in the West Pacific compared to regional and global paleoclimate and paleoceanographic reconstructions since 11 Ma. a Stack sea surface temperature (SST) anomalies for the Northern Hemisphere (NH), Southern Hemisphere (SH), and tropical[1]. **b** $^3He_{ET}$-derived opal fluxes and $^3He_{ET}$-derived Ba_{xs} fluxes from ODP 885/886[92]. **c** Nutrient utilization and productivity records Ba_{EF} at Sites U1425[38]. **d** P/Fe ratio in crust MID03 (this study). **e** Opal flux from East Pacific ODP Site 849[40]. **f** $CaCO_3$ accumulation rate from the three ocean basins[93]. **g** Paleoproductivity at ODP Site 1088 from the Southern Ocean[41]. **h** Redox-sensitive metals (normalized Ni, Mn, Cu composition) and anhysteretic remanent magnetization (ARM), as proxies for the relative magnetofossil abundance in crust MID03 (this study). **i** Foraminifera-bound $\delta^{15}N$ and reconstructed $[PO_4^{3-}]$ based on the P and Fe contents at DSDP Site 598[15].

https://doi.org/10.1038/s41467-025-56477-7

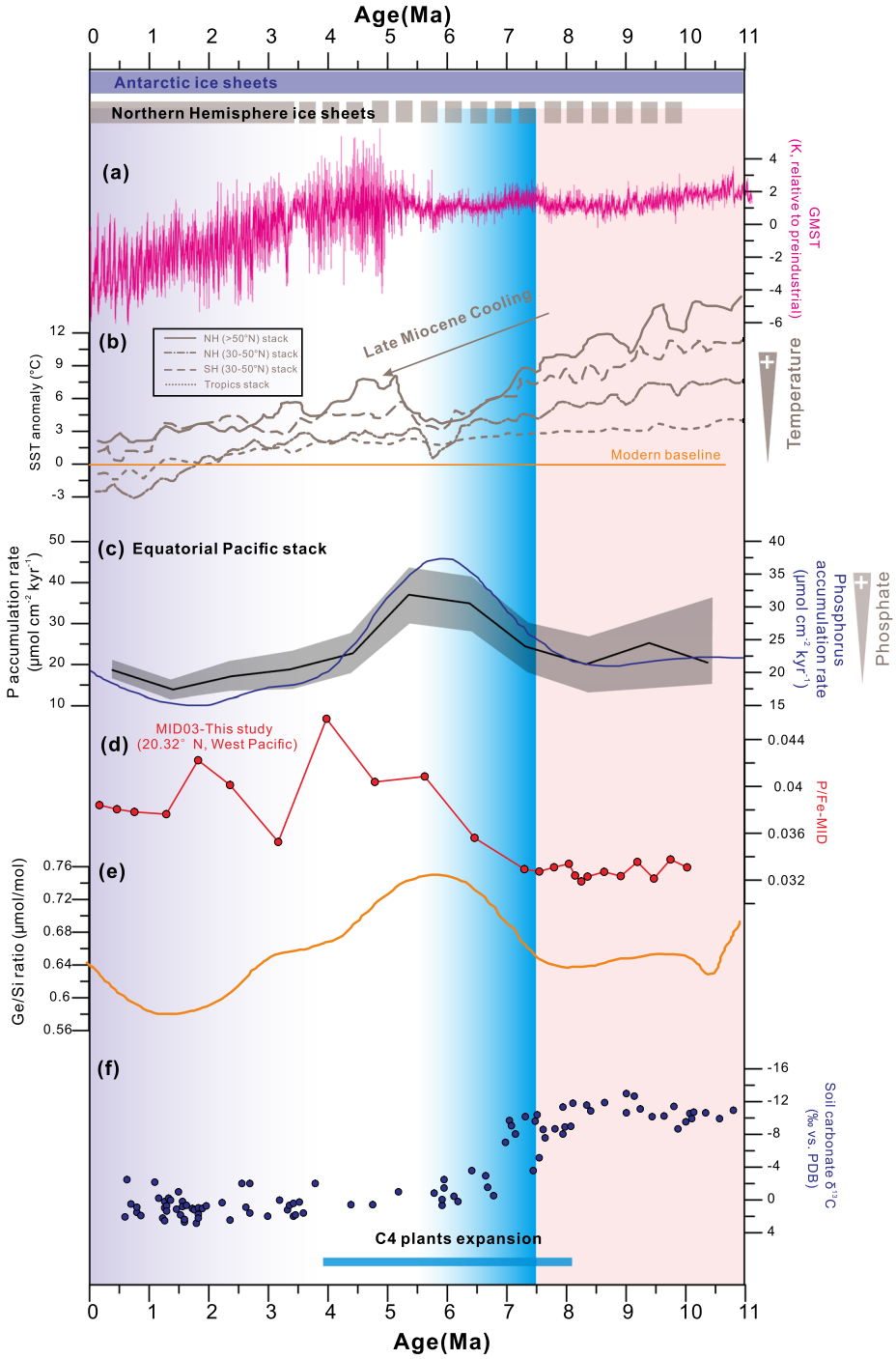

Fig. 3 | Compiled global and regional palaeoclimatic indicators of the past 11 Myr. a Global mean surface temperatures (GMST) estimated from benthic $\delta^{18}O$ data based on complied from ocean drilling core sites[94]. **b** Sea Surface Temperature (SST) compilation over the past 11 Myr[1]. **c** Phosphorus accumulation rate (μmol cm^{-2} kyr^{-1}) in the equatorial Pacific Ocean[36,37]. **d** P/Al ratio in crust MID03 (this study). **e** Ge/Si ratio in opaline silca from diatoms[75]. **f** Soil carbonate $\delta^{13}C$ from northern Pakistan[95]; vertical blue bars show the standard view of the presence and extent of full-scale/permanent ice sheets (solid bars) and those thought to have been partial/ephemeral (broken bars). The timing of C4 plant expansion is indicated at the base[14].

the ocean, which, together with elevated oceanic phosphorus concentrations, further stimulated primary productivity and phosphogenesis.

Moreover, the increase in oceanic P concentration could be closely connected with oceanic redox changes during the Late Miocene. Concurrent with the rise in oceanic P at ~7.5 Ma at the West Pacific site MID03 (Fig. 2d), a relative reduction of our measured oxygen-sensitive index in each subsample[59] (calculated following the method of ref. 59) of crust MID03 indicates a simultaneous decrease in bottom water oxygen concentrations (Fig. 2h and Supplementary Fig. 5c). We have also measured the anhysteretic remanent magnetization (ARM) of the crust MID03, which is a proxy of the magnetotactic bacteria (MTB). The results (Fig. 2h and Supplementary Fig. 6) indicate the presence of MTB, further supporting a decrease in bottom water oxygen concentrations, as suboxic conditions inhibit aerophilic MTB biomineralization[34]. This occurred

https://doi.org/10.1038/s41467-025-56477-7

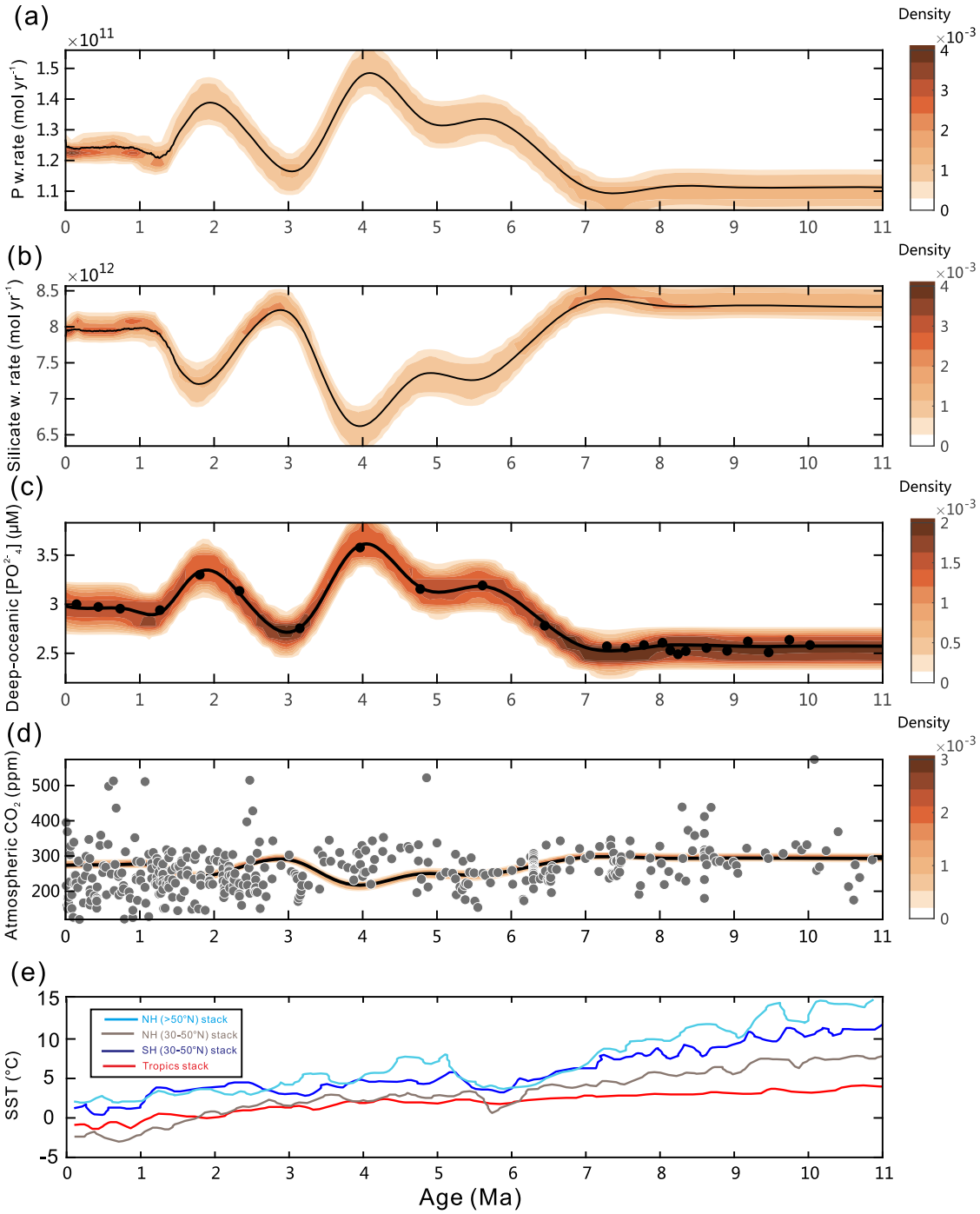

Fig. 4 | Evolution of simulated oceanic P contents and atmospheric pCO_2 along with reconstructed sea surface temperature (SST) over the last 11 Myr. a Model results for P weathering rate. **b** Model results for silicate weathering rate. **c** Oceanic P content. Model result of the deep ocean box (solid line). The points are calculated from the P/Fe data of this study using a linear scale factor, with the modern oceanic P concentration calibrated at 3 μM[84]. **d** Atmospheric pCO_2. Model result (solid line) compared with proxy data (open circles)[68]. **e** Reconstructed SST[1] from different latitudes. In this study, a Monte Carlo method was employed by varying the P weathering flux and climate sensitivity. A 5% variation was introduced to the P weathering flux using a normal distribution, while climate sensitivity was adjusted within a range of 4–6 °C also using a normal distribution. An enhancement factor of P weathering was applied to this simulation (Scenario 1), which is shown in Supplementary Fig. 8. Other than the enhanced forcing factor for P weathering, the other forcings include uplift as fixed at modern levels.

despite surface ocean cooling (Fig. 3a)[1] and intensified ocean circulation (Supplementary Fig. 7b)[36], attesting to enhanced deep-water deoxygenation in the Pacific Ocean in the Late Miocene[15]. Our results suggest that the amplified oceanic P fertilization effect and resultant higher biological production have outweighed this oceanic vertical mixing, leading to Pacific Ocean deoxygenation during the Late Miocene.

Dominant role of phosphorus fertilization in driving CO_2 consumption

The Late Miocene (~11.6–5.3 Ma) witnessed significant climatic, tectonic, and environmental changes at a global scale[5,10,60]. This time interval was characterized by more intense, high-latitude cooling and glacial events as well as by atmospheric CO_2 decline[61]. However, discerning the forcing behind these changes remains unresolved[2]. Asian

monsoon studies suggest that chemical weathering, including both silicate and P weathering linked to Neogene crustal exhumation, played a pivotal role in reducing atmospheric CO_2[17,20]. It has been proposed that this additional sink might have contributed to the substantial consumption of atmospheric CO_2 and the rapid global cooling observed in the Late Miocene[16].

Although both silicate and P weathering can lead to the consumption of atmospheric CO_2, the relative importance of these two processes on climate dynamics has not been established[62,63]. For instance, elevated P weathering linked to volcanic eruptions has been proposed as the driver for climate change during the Late Ordovician[64]. However, P and silicate weathering can be decoupled as P is primarily hosted in apatite and organic phases and may exhibit different reaction kinetics compared to silicates[65]. To assess the impact of P weathering on primary productivity and CO_2 consumption during the Late Miocene, we use a global biogeochemical model[66,67] and compare it to our reconstructed record of ocean P levels. The model is calibrated using contemporary biogeochemical fluxes, ocean circulation patterns, reservoir sizes, and seawater ion concentrations[66,67]. Our model results reveal decoupled P and silicate weathering regime across the Late Miocene.

First, we conducted model simulations by introducing a forced increase in P weathering using an enhancement factor (Supplementary Fig. 8), which was adjusted to match the observed changes in oceanic P concentrations. The results reveal that a ~30% rise in continental P weathering is required to produce the reconstructed peak oceanic P concentration at 4 Ma (Fig. 4c). This would lead to a significant ~60 ppm drop in atmospheric CO_2 during the Late Miocene, effectively explaining all of the change in atmospheric CO_2 record over this interval[68] (Fig. 4d). Next, to explore the impact of coupled enhanced silicate and P weathering, we conducted a set of model simulations with a forced increase in both P and silicate weathering using the same enhancement factor (Supplementary Fig. 9) or directly scaled the rates of P and silicate weathering (Supplementary Fig. 10). When adjusted to match our P/Fe record, the simulation with a forced increase in both P and silicate weathering using the same enhancement factor results in a decrease in atmospheric CO_2 from ~300 ppm to less than 150 ppm (Supplementary Fig. 9), a magnitude far too large to be reconciled with our proxy records (Fig. 4b). In the simulation with scaled P and silicate weathering, the model fails to reproduce the observed shift in seawater P concentration (Supplementary Fig. 10). This occurs because fully coupled P and silicate weathering should be balanced with degassing[69], and thus, with a fixed degassing rate, significant changes are unlikely. Consequently, our P/Fe record, along with the global biogeochemical model, do not support a coupled shift in P and silicate weathering. Currently, continental margin sediments account for about half of the total reactive P buried in the ocean[70]. We speculate that sea-level change in the Late Miocene influenced the global ocean P cycle because the fraction of P eroded from shelf sediments was prone to transport to the open ocean[65]. This substantiates the predominant role of enhanced P weathering in contributing to the late Miocene cooling.

Considering the nature and timing of significant climatic and tectonic events in Asia, we posit that regional tectonic-induced P weathering[71] was the primary trigger for the rapidly cooling climate and ice-sheet expansion along West Antarctica and in the Arctic by ~7 Ma (Fig. 3a and Supplementary Fig. 7a)[72]. The uplift and weathering of the Himalayan-Tibetan Plateau, as well as the Andes, may have accelerated the net flux of the bio-limiting nutrient phosphorus to the ocean, which is also supported by a noteworthy rise in P burial flux within marine sedimentary records (Fig. 3c and d)[73,74]. In this case, the temporary increase in nutrient input to the ocean accelerated dissolved element fluxes to the ocean and enhanced global oceanic productivity (Fig. 3e)[75]. Several mechanisms contribute to amplifying P weathering flux compared to silicate weathering through mountain uplift. Firstly, the elevation of mountains triggers a surge in soil erosion[76], delivering a significant amount of reactive particulate P to the ocean[77]. This P can subsequently be released as dissolved P during diagenetic regeneration[77]. Secondly, extensive exposure to P-rich basic volcanic rocks in regions such as the Tibetan Plateau and the Andes results in enhanced P weathering relative to silicate weathering[78]. Exposure of sea-level lowlands due to initial cooling can further intensify the erosion of unconsolidated sediments, facilitating the transport of reactive particulate P to the ocean[65].

Large-scale changes in terrestrial environments and ecosystems in subtropical and tropical regions[1] possibly played a crucial role in elevating P inputs into the ocean. We note that the timing of this P shift corresponds with a global benthic $\delta^{13}C$ decline and the expansion of C4 plants in subtropical regions occurred between 8 and 6 Ma (Fig. 3e)[13]. It has been postulated that such expansion altered the properties of land surface (e.g., increased the proportion of less dense grasslands), leading to greater soil erosion and higher soil organic matter input to the oceans[79]. As soil organic matter contains a significant amount of P, the remineralization of soil organic carbon would have also increased P input into the ocean, leading to a transient imbalance between input and export of P from the marine reservoir.

In summary, our data provide evidence for a persistent step-like increase in dissolved marine phosphate concentrations during the Late Miocene. Our findings suggest a prominent decoupling between P and silicate weathering during the LMC, highlighting the significance of terrestrial environmental and ecosystem changes in regulating P weathering and climate change. Our results provide a more comprehensive understanding of past oceanic nutrient variability and associated changes in weathering and climate impacts over the Cenozoic. Multiple P/Fe records from global crust samples would be helpful to further validate the shift in marine phosphate concentrations. Moreover, future high-resolution proxy studies may shed light on short-term changes in P weathering since the Miocene, and the importance of P weathering relative to silicate weathering during earlier global cooling episodes in Earth's history.

Methods

Age model

A total of seven micro-drilled Fe-Mn oxide samples were taken from the upper 50 mm of crust MID03, with a 2 mm layer thickness sample (Supplementary Fig. 2a). Subsample processing and Be isotopic measurements were carried out at the Xi'an Accelerator Mass Spectrometry Center (Xi'an-AMS Center), Institute of Earth Environment, Chinese Academy of Sciences. Seven subsamples were pretreated according to the protocol proposed by ref. 80 and updated by ref. 81. $^{10}Be/^{9}Be$ ratios were calibrated against ICN-01-5-1 material, using a certified ratio of $2.709 \times 10^{[-11}$ [82]. All the results (including correction for procedural blanks) are presented in Supplementary Table 2, and the resulting age models are shown in Supplementary Fig. 2. The subsamples display a continuous decline in $^{10}Be/^{9}Be$ with increasing depth in the crust from 0 to 37 mm (Supplementary Fig. 2b). Average growth rates and ages were calculated based on linear interpolation between those data points (Supplementary Fig. 2c), with growth rates between 2.5 and 8.3 mm/Ma being higher than the typical range of 1–5 mm/Ma for central Pacific crusts[83].

Element concentration measurements

The Fe-Mn MID03 crust was cut vertically at 1-2 mm intervals, and a total of 25 subsamples were scraped continuously from top to bottom for major and minor element analyses. Major elements were determined using a Thermo-Fisher IRIS II Intrepid XSP ICP-OES. Additional trace elements, including rare earth elements and yttrium (REY), were analyzed by inductively coupled plasma mass spectrometry using a Perkin-Elmer ELAN 9000 ICP-MS at Qingdao Sparta Analysis & Test

Co., Ltd. in China. The dissolution procedure was as follows: 0.05 g of sample powder was digested in a sealed Teflon beaker with 0.5 ml HF, 0.5 ml HNO_3, and 1.5 ml HCl on a hot plate (120 °C) for ~12 h. Following heating to dryness, 1 ml HNO_3 and 1 ml H_2O were added, and the beaker was sealed and heated on a hot plate (150 °C) for ~12 h to dissolve the residue. For internal calibration, we use the reference material GBW07315, GBW07316, BCR-2, BHVO-2, GBW07295, GBW07296, NOD-P-1, and NOD-A-1. Reference materials and parallel sample analysis are used for quality control during analysis. For major elements, the error range of the reference materials between the test value and the reference value is within 5%, and the accuracy can reach 95%. The relative standard deviation (RSD) of repeated analysis of this batch of samples was less than 2.5%. Estimated changes in oceanic P concentration are calculated from the P/Fe data of this study using a linear scale factor (Fig. 4), with modern oceanic P concentration calibrated at 3 μM[84].

Nd isotope measurements

Nd isotopes were analyzed on the Nu Plasma HR MC-ICP-MS with a DSN-100 desolvation nebulizing system, using a three-cycle dynamic procedure. Instrument bias and mass fractionation were corrected by normalization of raw ratios to $^{146}Nd/^{144}Nd = 0.7219$. Eleven measurements of JNdi-1 yield an average $^{143}Nd/^{144}Nd = 0.512113 \pm 9$ ($n = 11$), which is consistent with consensus value: 0.512115 ± 7. Lab standard Ames Nd Metal was used as a rotary instrument drift monitor, which corresponded with JNDi-1. 17 analyses yield an average of $^{143}Nd/^{144}Nd = 0.511966 \pm 16$; this value was used as a calibration reference for instrument drift, which is usually less than 15 ppm.

Mineral magnetic measurements

The subsamples were dried in an oven at a temperature below 40 °C and then placed in $2 \times 2 \times 2\ cm^3$ nonmagnetic plastic cubes to conduct magnetic measurements. Low- and high-frequency mass-specific magnetic susceptibility (χ_{lf} and χ_{hf}) were measured using a multifunction Kappabridge (MFK-FA) with frequencies of 976 Hz and 15,616 Hz, respectively. An alternating field (AF) was applied to each sample using a D-2000 AF demagnetizer, using a peak field of 100 mT and a direct current (DC) bias field of 0.05 mT, to obtain the anhysteretic remanent magnetization (ARM), which is regarded as representative of the stable single-domain (SD) ferrimagnetic content[85]. The susceptibility of anhysteretic remanent magnetization (χ_{ARM}) was obtained by dividing the ARM by the DC bias (0.05 mT). Saturation isothermal remanent magnetization (SIRM) was imparted to the Z-axis for each sample in a DC field of 1 T using an IM-10-30 Impulse Magnetizer and was measured using a JR-6A Spinner Magnetometer (AGICO). This SIRM, named $SIRM_{1T}$, was subsequently demagnetized with backfields of -100 and -300 mT, and the corresponding remanences (IRM_{-100mT} and IRM_{-300mT}, respectively were measured). Hysteresis loops and first-order reversal curves (FORCs) were measured up to maximum applied fields of 1.0 T for samples using a vibrating sample magnetometer (VSM, LakeShore 8600). The saturation magnetization (M_s) and coercivity (B_c) were obtained after high-field slope correction. The remanence coercivity (B_{cr}) was obtained by direct current demagnetization of $SIRM_{1T}$ back to -1.0 T. For every sample, a total of 100 FORCs measured with an averaging time of 500 ms and a maximum field of 400 mT were averaged. The FORC diagrams were processed using the software 'FORCinel'[86] with VARIFORC smoothing[87]. Principle component analysis (FORC-PCA) was also performed using 'FORCinel' following the protocols of ref. 88. Magnetic measurements were performed at the Center for Marine Magnetism (CM^2), Southern University of Science and Technology in China.

Model simulations

The global biogeochemical model utilized in this study is derived from[66,67] and encompasses the cycling of carbon, oxygen, phosphorus, iron, and sulfur through five oceanic boxes and one atmospheric box (Supplementary Tables 5–8). For an in-depth understanding of the model, please refer to refs. 66,67.

For the simulations aimed at assessing the isolated impact of a prescribed rise in phosphorus (P) weathering on oceanic P concentration and climate, we introduced an enhancement factor for P weathering (Supplementary Fig. 8), which was tuned to mach the observed changes in oceanic P concentrations. It is important to note that in this particular simulation, we maintained the formulas for silicate and carbonate weathering without alteration. The formulas for silicate weathering and carbonate weathering were consistent with those outlined in ref. 66, relying on functions of temperature and runoff.

In the model run designed to simulate the combined effects of P and silicate weathering, we applied the same enhancement factor (Supplementary Fig. 8) to P, silicate, and carbonate weathering. This approach ensures a comprehensive examination of the integrated impact of these processes on oceanic P concentration and climate dynamics.

Data availability

All data needed to evaluate the conclusions in the paper are present in the paper and/or Supplementary Material. The proxy data are available in https://doi.org/10.5281/zenodo.10801796 during this study. The other data that support the findings of this study are included in the Supplementary information files.

References

1. Herbert, T. D. et al. Late Miocene global cooling and the rise of modern ecosystems. *Nat. Geosci.* **9**, 843–847 (2016).
2. Holbourn, A. E. et al. Late Miocene climate cooling and intensification of southeast Asian winter monsoon. *Nat. Commun.* **9**, 1584 (2018).
3. Rae, J. W. B. et al. Atmospheric CO_2 over the Past 66 Million Years from Marine Archives. *Annu. Rev. Earth Planet. Sci.* **49**, 609–641 (2021).
4. Westerhold, T. et al. An astronomically dated record of Earth's climate and its predictability over the last 66 million years. *Science* **369**, 1383–1387 (2020).
5. Zhang, Y. G., Pagani, M. & Liu, Z. A 12-Million-year temperature history of the tropical pacific ocean. *Science* **344**, 84–87 (2014).
6. Beerling, D. J. et al. Enhanced chemistry-climate feedbacks in past greenhouse worlds. *Proc. Natl. Acad. Sci. USA* **108**, 9770–9775 (2011).
7. Isson, T. T. et al. Evolution of the global carbon cycle and climate regulation on earth. *Glob. Biogeochem. Cycle* **34**, e2018GB006061 (2020).
8. Tierney, J. E. et al. Glacial cooling and climate sensitivity revisited. *Nature* **584**, 569–573 (2020).
9. Tierney, J. E. et al. Spatial patterns of climate change across the Paleocene–Eocene Thermal Maximum. *Proc. Natl. Acad. Sci. USA* **119**, e2205326119 (2022).
10. LaRiviere, J. P. et al. Late Miocene decoupling of oceanic warmth and atmospheric carbon dioxide forcing. *Nature* **486**, 97–100 (2012).
11. Wen, Y. et al. CO_2-forced Late Miocene cooling and ecosystem reorganizations in East Asia. *Proc. Natl. Acad. Sci. USA* **120**, e2214655120 (2023).
12. Cerling, T. E., Wang, Y. & Quade, J. Expansion of C4 ecosystems as an indicator of global ecological change in the late Miocene. *Nature* **361**, 344–345 (1993).
13. Polissar, P. J. et al. Synchronous rise of African C4 ecosystems 10 million years ago in the absence of aridification. *Nat. Geosci.* **12**, 657–660 (2019).

14. Du, J., Tian, J. & Ma, W. The late miocene carbon isotope shift driven by synergetic terrestrial processes: A box-model study. *Earth Planet. Sci. Lett.* **584**, 117457 (2022).
15. Wang, X. T. et al. Oceanic nutrient rise and the late Miocene inception of Pacific oxygen-deficient zones. *Proc. Natl. Acad. Sci. USA* **119**, e2204986119 (2022).
16. Yang, Y. et al. Monsoon-enhanced silicate weathering as a new atmospheric CO_2 consumption mechanism contributing to fast late miocene global cooling. *Paleoceanogr. Paleoclimatol.* **36**, https://doi.org/10.1029/2020PA004008 (2021).
17. Clift, P. D. et al. Correlation of Himalayan exhumation rates and Asian monsoon intensity. *Nat. Geosci.* **1**, 875–880 (2008).
18. Isson, T. T. & Planavsky, N. J. Reverse weathering as a long-term stabilizer of marine pH and planetary climate. *Nature* **560**, 471–475 (2018).
19. Kump, L. R., Brantley, S. L. & Arthur, M. A. Chemical weathering, atmospheric CO_2, and climate. *Annu. Rev. Earth Planet. Sci.* **28**, 611–667 (2000).
20. Wan, S. et al. Enhanced silicate weathering of tropical shelf sediments exposed during glacial lowstands: A sink for atmospheric CO_2. *Geochim. Cosmochim. Acta* **200**, 123–144 (2017).
21. Isson, T. & Rauzi, S. Oxygen isotope ensemble reveals Earth's seawater, temperature, and carbon cycle history. *Science* **383**, 666–670 (2024).
22. Tyrrell, T. The relative influences of nitrogen and phosphorus on oceanic primary production. *Nature* **400**, 525–531 (1999).
23. Bergman, N. M., Lenton, T. M. & Watson, A. J. COPSE: a new model of biogeochemical cycling over Phanerozoic time. *Am. J. Sci.* **304**, 397–437 (2004).
24. Wallmann, K. Feedbacks between oceanic redox states and marine productivity: A model perspective focused on benthic phosphorus cycling. *Global Biogeochem. Cycles* **17**, 1084 (2003).
25. Elser, J. J. et al. Global analysis of nitrogen and phosphorus limitation of primary producers in freshwater, marine and terrestrial ecosystems. *Ecol. Lett.* **10**, 1135–1142 (2007).
26. Föllmi, K. B. The phosphorus cycle, phosphogenesis and marine phosphate-rich deposits. *Earth Sci. Rev.* **40**, 55–124 (1996).
27. Howarth, R. W. Nutrient limitation of net primary production in marine ecosystems. *Annu. Rev. Ecol. Syst.* **19**, 89–110 (1988).
28. Guo, L. et al. Acceleration of phosphorus weathering under warm climates. *Sci. Adv.* **10**, eadm7773 (2024).
29. Bjerrum, C. J. & Canfield, D. E. Ocean productivity before about 1.9 Gyr ago limited by phosphorus adsorption onto iron oxides. *Nature* **417**, 159–162 (2002).
30. Feely, R. A. et al. The relationship between P/Fe and V/Fe ratios in hydrothermal precipitates and dissolved phosphate in seawater. *Geophys. Res. Lett.* **25**, 2253–2256 (1998).
31. Koschinsky, A. & Halbach, P. Sequential leaching of marine ferromanganese precipitates: Genetic implications. *Geochim. Cosmochim. Acta* **24**, 5113–5132 (1995).
32. Koschinsky, A. et al. Effects of phosphatization on the geochemical and mineralogical composition of marine ferromanganese crusts. *Geochim. Cosmochim. Acta* **61**, 4079–4094 (1997).
33. Garcia, H. E. et al. World Ocean Atlas 2023, Volume 4: Dissolved Inorganic Nutrients (phosphate, nitrate, silicate) NOAA Atals NESDIS 92 (2024).
34. Jiang, X. D. et al. Abyssal manganese nodule recording of global cooling and tibetan plateau uplift impacts on Asian aridification. *Geophys. Res. Lett.* **49**, e2021GL096624 (2022).
35. Filippelli, G. M. & Delaney, M. L. The oceanic phosphorus cycle and continental weathering during the Neogene. *Paleoceanogr. Paleoclimtol.* **9**, 643–652 (1994).
36. Moody, J. B., Chaboudy, J. L. R. & Worsley, T. R. Pacific pelagic phosphorus accumulation during the last 10 M. *Y. Paleoceanography* **3**, 113–136 (1988).
37. Fillippelli, G. M. & Delaney, M. L. The globoal phosphorus cycle: Past, present, and future. *Elements* **4**, 89–95 (2008).
38. Zhai, L. et al. Deep-water formation in the North Pacific during the late miocene global cooling. *Paleoceanogr. Paleoclimatol.* **36**, e2020PA003946 (2021).
39. Zhang, Y. G. et al. A long history of equatorial deep-water upwelling in the Pacific Ocean. *Earth Planet. Sci. Lett.* **467**, 1–9 (2017).
40. Farrell, J. W. et al. Late Neogene sedimentation patterns in the eastern equatorial Pacific Ocean. *Proceedings of the Ocean Drilling Program, scientific results* **138**, (1995).
41. Diekmann, B., Fälker, M. & Kuhn, G. Environmental history of the south-eastern South Atlantic since the Middle Miocene: evidence from the sedimentological records of ODP Sites 1088 and 1092. *Sedimentology* **50**, 511–529 (2003).
42. Lyle, M. & Baldauf, J. Biogenic sediment regimes in the Neogene equatorial Pacific, IODP Site U1338: Burial, production, and diatom community. *Paleogeogr. Paleoclimatol. Paleoecol.* **433**, 106–128 (2015).
43. Weber, M. E. et al. Carbonate preservation history in the Peru Basin: Paleoceanographic implications. *Paleoceanogr. Paleoclimatol.* **10**, 775–800 (1995).
44. Zhao, M. et al. The role of calcium in regulating marine phosphorus burial and atmospheric oxygenation. *Nat. Commun.* **11**, 2232 (2020).
45. Letelier, R. M. et al. Climate-driven oscillation of phosphorus and iron limitation in the North Pacific Subtropical Gyre. *Proc. Natl. Acad. Sci.USA* **116**, 12720–12728 (2019).
46. Yuan, Z. W. et al. Potential drivers and consequences of regional phosphate depletion in the western subtropical North Pacific. *Limnol. Oceanogy. Lett.* https://doi.org/10.1002/lol2.10314 (2023).
47. Hein, J. R. et al. Two major Cenozoic episodes of phosphogenesis recorded in equatorial Pacific seamount deposits. *Paleocean* **8**, 293–311 (1993).
48. Peng, J. Z. et al. Episodic intensification of marine phosphorus burial over the last 80 million years. *Nat. Commun.* **15**, 7446 (2024).
49. Glasby, G. P. & Summerhayes, C. P. Sequential deposition of authigenic marine minerals around New Zealand: Paleoenvironmental significance: New Zealand. *J. Geol. Geophys.* **18**, 4770490 (1975).
50. Glasby, G. P. & Wright, I. C. Marine mineral potential in New Zealand's exclusive economic zone. In *Proceedings of the Annual Offshore Technology Conference,* 479–490 (1990).
51. Manheim, F. T., Pratt, R. M., & McFarlin, P. F. in *Marine Phosphorites — Geochemistry, Occurrence, Genesis*, (ed. Bentor, Y. K.) 117–137 (SEPM Special Publication, 11980).
52. Siesser, W. G. Age of phosphorites on the South African continental margin. *Mar. Geol.* **26**, M17–M28 (1978).
53. González, F. J. et al. Martín-Rubí, phosphorites, co-rich Mn nodules, and Fe-Mn crusts from Galicia bank, NE Atlantic: Reflections of Cenozoic tectonics and paleoceanography. *Geochem. Geophys. Geosyst.* **17**, 346–374 (2016).
54. Mullins, H. T. & Rasch, R. F. Sea-floor phosphorites along the central Califorrnia continental margin. *Econ. Geol.* **80**, 696–715 (1997).
55. Schollhorn, I. et al. Enhanced upwelling and phosphorite formation in the northeastern Pacific during the late Oligocene: Depositional mechanisms, environmental conditions, and the impact of glacioeustacy. *Geol. Soc. Am. Bull.* **132**, 687–709 (2020).
56. Hu, R., Chen, T. & Ling, H. Late Cenozoic history of deep water circulation in the western North Pacific: Evidence from Nd isotopes of ferromanganese crusts. *Chin. Sci. Bull.* **57**, 4077–4086 (2012).

57. Ling, H. F. et al. Evolution of Nd and Pb isotopes in Central Pacific seawater from ferromanganese crusts. *Earth Planet. Sci. Lett.* **146**, 1–12 (1997).
58. Liu, R. et al. Isotopic fingerprinting of dissolved iron sources in the deep western Pacific since the late Miocene. *Sci. China Earth Sci.* **63**, 1767–1779 (2020).
59. Yi, L. et al. Plio-Pleistocene deep-sea ventilation in the eastern Pacific and potential linkages with Northern Hemisphere glaciation. *Sci. Adv.* **9**, eadd1467 (2023).
60. Tanner, T. et al. Decreasing atmospheric CO_2 during the Late Miocene cooling. *Paleoceanogr. Paleoclimatol.* **35**, e2020PA003925 (2020).
61. Si, W. & Rosenthal, Y. Reduced continental weathering and marine calcification linked to late Neogene decline in atmospheric CO_2. *Nat. Geosci.* **12**, 833–838 (2019).
62. Raymo, M. E. Geochemical evidence supporting TC Chamberlin's theory of glaciation. *Geology* **19**, 344–347 (1991).
63. Raymo, M. E., Ruddiman, W. F. & Froelich, P. N. Influence of late Cenozoic mountain building on ocean geochemical cycles. *Geology* **16**, 649–653 (1988).
64. Longman, J. et al. Late Ordovician climate change and extinctions driven by elevated volcanic nutrient supply. *Nat. Geosci.* **14**, 924–929 (2021).
65. Ruttenberg, K. C. Reassessment of the oceanic residence time of phosphoru. *Chem. Geol.* **107**, 405–409 (1993).
66. Zhao, M. et al. Oxygenation of the Earth aided by mineral–organic carbon preservation. *Nat. Geosci.* **16**, 262–267 (2023).
67. Zhao, M. et al. Drivers of the global phosphorus cycle over geological time. *Nat. Rev. Earth Environ.* **5**, 873–889 (2024).
68. Cui, Y., Schubert, B. A. & Jahren, A. H. A 23 my record of low atmospheric CO_2. *Geology* **48**, 888–892 (2020).
69. Berner, R. A. & Caldeira, K. The need for mass balance and feedbaack in the geochemical carbon cycle. *Geology* **25**, 955–956 (1997).
70. Compton, J. S. et al. Origin and age of phosphorite from the South-central Florida Platform: Relation of phosphogenesis to sea-level fluctuation and $\delta^{13}C$ excursions. *Geochim. Cosmochim. Acta.* **57**, 131–146 (1993).
71. Miao, Y. et al. A new biologic paleoaltimetry indicating Late Miocene rapid uplift of northern Tibet Plateau. *Science* **378**, 1074–1079 (2022).
72. Zachos, J. et al. Trends, rhythms, and aberrations in global climate 65 Ma to present. *Science* **292**, 686–693 (2001).
73. Filippelli, G. M. Intensification of the Asian monsoon and a chemical weathering event in the late Miocene–early Pliocene: Implications for late Neogene climate change. *Geology* **25**, 27–30 (1997).
74. Filippelli, G. M. The global phosphorus cycle: Past, present, and future. *Elements* **4**, 89–95 (2008).
75. Shemesh, A., Mortlock, R. A. & Froelich, P. N. Late Cenozoic Ge/Si record of marine biogenic opal: Implications for variations of riverine fluxes to the ocean. *Paleoceanography* **4**, 221–234 (1989).
76. Goddéris, Y. et al. Onset and ending of the late Palaeozoic ice age triggered by tectonically paced rock weathering. *Nat. Geosci.* **10**, 382–386 (2017).
77. Berner, R. A. & Rao, J. L. Phosphorus in sediments of the Amazon river and estuary-implications for the global flux of phosphorus to the sea. *Geochim. Cosmochim. Acta* **58**, 2333–2339 (1994).
78. Hartmann, J. et al. Global chemical weathering and associated P-release—The role of lithology, temperature and soil properties. *Chem. Geol.* **363**, 145–163 (2014).
79. Diester-Haass, L., Billups, K. & Emeis, K. C. Late Miocene carbon isotope records and marine biological productivity: Was there a (dusty) link? *Paleoceanogr. Paleoclimatol.* **21**, https://doi.org/10.1029/2006PA001267 (2006).
80. Bourlès, D. L. et al. Beryllium in marine pore waters: geochemical and geochronological implications. *Nature* **341**, 731–733 (1989).
81. Simon, Q. et al. Authigenic $^{10}Be/^{9}Be$ ratios and ^{10}Be-fluxes ($^{230}Th_{xs}$-normalized) in central Baffin Bay sediments during the last glacial cycle: Paleoenvironmental implications. *Quat. Sci. Rev.* **140**, 142–162 (2016).
82. Nishiizumi, K. et al. Absolute calibration of ^{10}Be AMS standards. *Nucl. Instrum. Methods Phys. Res.* **258**, 403–413 (2007).
83. Hein, J. R. et al. in *Handbook of Marine Mineral Deposits* (ed. Cronan, D. S.) 239–279 (CRC Press, 2000).
84. Levitus, S. et al. Distribution of nitrate, phosphate and silicate in the world oceans. *Prog. Oceanogr.* **31**, 245–273 (1993).
85. King, J. W. & Channell, J. E. Sedimentary magnetism, environmental magnetism, and magnetostratigraphy. *Rev. Geophys.* **29**, 358–370 (1991).
86. Harrison, R. J. & Feinberg, J. M. FORCinel: An improved algorithm for calculating first-order reversal curve distributions using locally weighted regression smoothing. *Geochem. Geophys. Geosyst.* **9**, 1–11 (2008).
87. Egli, R. VARIFORC: An optimized protocol for calculating non-regular first-order reversal curve (FORC) diagrams. *Glob. Planet. Change* **110**, 302–320 (2013).
88. Lascu, I. H., et al. Magnetic unmixing of first-order reversal curve diagrams using principal component analysis. *Geochem. Geophys. Geosyst.* **16**, 2900–2915 (2015).
89. Bell, D. B. et al. Local and regional trends in Plio-Pleistocene $\delta^{18}O$ records from benthic foraminifera. *Geochem. Geophys. Geosyst.* **15**, 3304–3321 (2014).
90. Kawabe, M. & Fujio, S. Pacific Ocean circulation based on observation. *J. Oceanogr.* **66**, 389–403 (2010).
91. Schliter, R. Ocean Data View. https://odv.awi.de (2021).
92. Abell, J. T. & Winckler, G. Long-term variability in Pliocene North Pacific Ocean export production and its implications for Ocean circulation in a Warmer World. *AGU Adv.* **4**, e2022AV000853 (2023).
93. Pillot, Q. et al. A global reassessment of the spatial and temporal expression of the late miocene biogenic bloom. *Paleoceanogr. Paleoclimatol.* **38**, e2022PA004564 (2023).
94. The Cenozoic CO_2 Proxy Integration Project ($CenCO_2PIP$) Consortium. Toward a Cenozoic history of atmospheric CO_2. *Science* **382**, 1136 (2023).
95. Cerling, T. E. et al. Global vegetation change through the Miocene/Pliocene boundary. *Nature* **389**, 153–158 (1997).

Acknowledgements

We thank the China Ocean Sample Repository for supplying samples. We thank Ann Holbourn and Qing Yan for their advice and discussions. This work was supported financially by the National Natural Science Foundation of China (grant 92158208, 42274094, 42261144739, 42304082, 42204082, and 42330403), Shenzhen Science and Technology Program (JCYJ20240813094216022 and KCXFZ20211020174803005) and the High-Level Special Fund of SUStech (G0305K001), M.Z. is funded by the programs of the Chinese Academy of Sciences (E32D53201, E32C530102 and XDA0430202).

Author contributions

Conceptualization: Y.Z., Q.S.L., and M.Y.Z. Methodology: J.L.D. and Z.G.L. Investigation: X.F.S. Visualization: H.L. and Q.Z. Writing——original draft: Y.Z., J.M.Y., and M.Y.Z. Writing——review and editing: T.I., S.K., Z.L., G.E.A.S., A.P., M.E.W., J.C.L., J.Y.Z., Y.F.S., F.J.G., S.K.B., D.B.Z., and W.C.

Competing interests

The authors declare no competing interests.

Additional information

Supplementary information The online version contains supplementary material available at https://doi.org/10.1038/s41467-025-56477-7.

Correspondence and requests for materials should be addressed to Yi Zhong, Mingyu Zhao or Qingsong Liu.

Peer review information *Nature Communications* thanks the anonymous reviewers for their contribution to the peer review of this work. A peer review file is available.

Reprints and permissions information is available at http://www.nature.com/reprints

Publisher's note Springer Nature remains neutral with regard to jurisdictional claims in published maps and institutional affiliations.

Open Access This article is licensed under a Creative Commons Attribution-NonCommercial-NoDerivatives 4.0 International License, which permits any non-commercial use, sharing, distribution and reproduction in any medium or format, as long as you give appropriate credit to the original author(s) and the source, provide a link to the Creative Commons licence, and indicate if you modified the licensed material. You do not have permission under this licence to share adapted material derived from this article or parts of it. The images or other third party material in this article are included in the article's Creative Commons licence, unless indicated otherwise in a credit line to the material. If material is not included in the article's Creative Commons licence and your intended use is not permitted by statutory regulation or exceeds the permitted use, you will need to obtain permission directly from the copyright holder. To view a copy of this licence, visit http://creativecommons.org/licenses/by-nc-nd/4.0/.

© The Author(s) 2025

[1]Centre for Marine Magnetism (CM2), Department of Ocean Science and Engineering, Southern University of Science and Technology, Shenzhen, China. [2]Advanced Institute of Ocean Research, Department of Ocean Scicence and Engineering, Southern University of Science and Technology, Shenzhen, PR China. [3]State Key Laboratory of Biogeology and Environmental Geology, School of Earth Sciences, China University of Geosciences, Wuhan, China. [4]Key Laboratory of Marine Sedimentology and Environmental Geology, First Institute of Oceanography, State Oceanic Administration, Qingdao, China. [5]Te Aka Mātuatua, University of Waikato (Tauranga), BOP, Tauranga, New Zealand. [6]Laoshan Laboratory, Qingdao, China. [7]Research School of Earth Sciences, Australian National University, Canberra, ACT, Australia. [8]SKLLQG, Institute of Earth Environment, Chinese Academy of Sciences, Xi'an, China. [9]Camborne School of Mines, Department of Earth and Environmental Sciences, University of Exeter, Cornwall, UK. [10]Department of Earth, Ocean and Atmospheric Science, Florida State University, Tallahassee, FL, USA. [11]School of Geography, University of Nottingham, Nottingham, UK. [12]Department of Environmental Engineering and Earth Sciences, Clemson University, Clemson, South Carolina, USA. [13]Institute for Geosciences, Department of Geochemistry and Petrology, University of Bonn, Bonn, Germany. [14]State Key Laboratory of Marine Geology, Tongji University, Shanghai, China. [15]Department of Science, Universidad Pública de Navarra, Campus de Arrosadia, Pamplona, Spain. [16]IGME, CSIC, Campus Aula Dei, Zaragoza, Spain. [17]Chinese Academy of Sciences Key Laboratory of Crust-Mantle Materials and Environments, University of Science and Technology of China, Hefei, China. [18]Geological Survey of Spain (IGME), Rios Rosas 23, Madrid, Spain. [19]Institute of Geological Sciences, Freie Universität Berlin, Berlin, Germany. [20]Southern Marine Science and Engineering Guangdong Laboratory (Guangzhou), Guangzhou, China. [21]School of Geophysics and Information Technology, China University of Geosciences, Beijing, China. [22]Key Laboratory of Marine Geology and Environment, Institute of Oceanology, Chinese Academy of Sciences, Qingdao, China. [23]State Key Laboratory of Lithospheric and Environmental Coevolution, Institute of Geology and Geophysics, Chinese Academy of Sciences, Beijing, China. [24]Shanghai Sheshan National Geophysical Observatory, Shanghai, China. ✉e-mail: zhongy@sustech.edu.cn; mingyu.zhao@mail.iggcas.ac.cn; qsliu@sustech.edu.cn